



Large-scale synthetic Mo@ (2H-1T)-MoSe₂ monolithic electrode for efficient hydrogen evolution in all pH scale ranges and seawater

Chunming Yang^{a,1}, Lihai Zhou^{a,1}, Chuantao Wang^{a,1}, Wen Duan^a, Le Zhang^a, Fuchun Zhang^a, Junjun Zhang^b, Yanzhong Zhen^{a,*}, Loujun Gao^{a,*}, Feng Fu^{a,*}, Yucang Liang^{c,*}

^a Shaanxi Key Laboratory of Chemical Reaction Engineering, School of Chemistry & Chemical Engineering, Yan'an University, Yan'an 716000, Shaanxi, China

^b School of Materials Science and Chemical Engineering, Xi'an Technological University, Xi'an 710021, Shaanxi, China

^c Institut für Anorganische Chemie, Eberhard Karls Universität Tübingen, Auf der Morgenstelle 18, 72076 Tübingen, Germany

ARTICLE INFO

Keywords:

Molybdenum diselenide
Heterojunction interface
Phase and morphology engineering
Hydrogen evolution reaction
Full pH

ABSTRACT

Although molybdenum selenide with controllable phase and morphology is pivotal for high-efficiency hydrogen evolution reaction (HER), at present, the MoSe₂-based HER electrodes widely applied to all pH scale ranges and seawater are remaining tremendous challenge, due to the absence of active sites, poor conductivity of MoSe₂ and the limitation of synthetic method. In this work, the large-scale Mo@ (2H-1T)-MoSe₂ monolithic electrode was successfully fabricated by etching Mo mesh in Na₂SeO₃ solution via a hydrothermal technique. Continuous phase and morphology modulation of MoSe₂ on Mo mesh and the optimal synthetic condition are described to fabricate a state-of-the-art electrode Mo@ (2H-1T)-MoSe₂ with the piezo-flexoelectric coupling effect and heterostructure. The HER tests of Mo@ (2H-1T)-MoSe₂ in all pH ranges and seawater exhibit an enhanced HER activity, high stability and cycle durability, which benefit from the synergistic interaction of the piezo-flexoelectric coupling effect of hybrid 2H-1T phase of MoSe₂ nanosheets and heterojunction. Operando EIS and theoretical calculations also revealed this viewpoint. This strategy can also be extended arbitrarily to the large-scale preparation of other heterostructured monolithic electrodes for high-efficiency HER, such as M@MSe_x (M = Ni, Cu, W, etc.). This study provides a simple, effective and low-cost approach to develop the state-of-the-art metal-based heterostructured electrodes for other energy-related applications.

1. Introduction

Energy is the fundamental driving force of world development and economic growth. With the gradual depletion of traditional fossil resources, the development of new clean alternative energy sources has gradually become a human consensus [1]. Hydrogen, a high calorific value, wide source, multiple utilization forms, cost-effective and non-polluting reaction product, is identified as an ideal clean and sustainable energy system [2]. Water splitting into hydrogen can be integrated with green energy power generation (e.g., solar and wind) to develop a new energy conversion and storage system. To achieve this goal, the developed electrocatalyst not only requires reducing the overpotential and accelerating the kinetics, but also demands working very well under acidic, basic and neutral conditions [3,4]. Nevertheless, the significant performance of most reported electrocatalysts is only restricted to extremely narrow pH scope and harsh acidic/alkaline

conditions, greatly limiting practical application. For example, under neutral, alkaline and natural seawater environment, hydrogen evolution encounters slow kinetics, which demands that electrocatalyst possesses an excellent activity for water adsorption and dissociation to produce hydrogen intermediates (H*) at rate-limiting Volmer step (H₂O + e⁻ → H* + OH⁻) of hydrogen evolution reaction (HER). Under an acidic condition, the durability of electrocatalyst should be taken into consideration. Moreover, direct electrolysis of inexhaustible seawater accounted for more than 96.5% of global water resources possesses great prospects in large-scale and low-cost production of nearly infinite hydrogen energy [5,6]. Hence, a rationally designed and successfully prepared an advanced and ideal electrode material is becoming imperative for HER process in all pH scale ranges and seawater.

In recent years, molybdenum selenide (MoSe₂) has become one of the research hotspots owing to its unique physical and chemical property [7–9]. Especially, the morphological and structural characteristics

* Corresponding authors.

E-mail addresses: zyz943@163.com (Y. Zhen), glj@yau.edu.cn (L. Gao), yadxufeng@126.com (F. Fu), yucang.liang@uni-tuebingen.de (Y. Liang).

¹ These authors contributed equally to this work.

of MoSe₂ often play pivotal roles to markedly influence catalytic performance [10], for example, the few-layered MoSe₂ nanosheets with abundant edge and high electrical conductivity displayed the strong piezo-flexoelectric coupling effect induced by the strain gradients at interfacial areas, on edge sites and on polarized surfaces of MoSe₂ nanosheets across the top and bottom surfaces for enhanced HER activity, while MoSe₂ with trigonal prismatic or octahedral lattice also indicated different catalytic activities for HER. MoSe₂ includes 2H phase (trigonal prismatic lattice, 2H-MoSe₂) and 1T phase (octahedral lattice, 1T-MoSe₂) [7–11], and in which the former is a stable n-type semiconductor with relatively low conductivity and catalytic performance and the later has a metastable metallic performance with better HER activities and it could be transformed to 2H-MoSe₂ [12]. Moreover, 2H phase of MoSe₂ can also be converted into 1T phase to produce biphasic-coexisted (1T-2H)-MoSe₂, which indicated an improved HER activity [13], proving that phase engineering is an effective strategy to improve the electrocatalytic activity of MoSe₂, due to that 1T phase MoSe₂ exposed more catalytically active sites [14]. In addition to phase engineering, heterojunction interface engineering in MoSe₂ has also been extensively investigated due to that different heterostructures could further boost physical-chemical property and electrocatalytic activity [15–18]. Furthermore, surface plasma functionalization, in-situ coalesced vacancies, surface electron accumulation, heteroatom modification and by introducing substrate layer with an abundant edge and high electrical conductivity also can increase the efficiency of MoSe₂ in HER [19–24]. Recently, benefiting from synergetic effects and enhanced electron transfer at the interface, Mott-Schottky catalysts are widely applied in energy storage and conversion [25]. When appropriate metal contacts with semiconductor, electron can flow spontaneously at such interfaces until the fermi level on both sides are equal, according to Mott-Schottky effect [26]. This flow of electrons effectively regulates the electron density on the surface of metals and semiconductors, and thereby promotes the ability of water adsorption and dissociation to produce hydrogen intermediates (H*). At present, in spite of the substantial progress in the construction of Mott-Schottky electrocatalyst, the reported synthetic methods are generally difficult to scale up production. For a lab-scale catalyst, the synthetic conditions can be precisely controlled and most electrocatalysts can be successfully prepared. However, with the expansion of the synthesis scale, the uneven mass transfer and heat transfer effects can easily cause catalyst to be difficult to prepare [27,28]. In addition, many synthesis methods are only suitable for the synthesis of one catalyst, and they can't be extended arbitrarily to the preparation of other catalysts. Thus, it is very pivotal and necessary to develop a facile, simple and expandable strategy for large-scale construction of Mott-Schottky electrocatalysts.

Recent years, the piezo-/flexoelectricity of nanosheet-based single atomic layered or few-layered two-dimensional transition metal dichalcogenides (2D TMD) including MoS₂ and MoSe₂ has attracted considerable attention [8,29–33]. Piezoelectric potential is caused by noncentrosymmetric structure [29,30] or created by the internal electric fields in different polarization domains of the single- and few-layered MoSe₂ [8] as well as the strains at interfacial areas between different phases [9]. Flexoelectric potential is induced by local defect sites, cracking edge-site defects, structural phase boundaries and strain gradient-driven lattice distortion in the structural phase boundaries confirmed by theoretical calculation, which highly depended on size and bending moment of the few-layered MoSe₂ nanosheets [9]. Note that piezoelectricity not only exists in 2D TMDs but also in other material [34]. The piezoelectricity and flexoelectricity of materials and their piezo- and flexopotential coupling effect strongly influence catalytic behaviors.

In this work, we report an efficient and facile hydrothermal in situ etching method to fabricate large-scale Mott-Schottky heterojunction Mo@(2H-1T)-MoSe₂ monolithic electrode, and this strategy can be arbitrarily extensible to the preparation of other catalysts such as M@MSe_x (M = Ni, Cu, W etc.). The phase and morphology engineering

of MoSe₂ can be readily performed by adjusting the reaction conditions, such as concentration of Na₂SeO₃, temperature and time. Such Mo@(2H-1T)-MoSe₂ electrode in HER showed the high catalytic activities, high stability and cycle durability in all pH scale ranges (0.5 M H₂SO₄, 1 M KOH, 1 M PBS) and seawater, fulfilling the key-requirements for practical applications in all kinds of media. Furthermore, the synergistic effect of piezo-flexoelectric coupling 2H-1T phase of MoSe₂ and heterojunction interface unveils the structure-property relationship. This strategy provides a facile and efficient approach to fabricate the large-scale electrocatalysts metal-metal selenide with heterostructure for the practical industrial application in HER even OER.

2. Experimental section

2.1. Materials

Sodium selenite (Na₂SeO₃) and hydrochloric acid solution (HCl, 36–38 wt%) were purchased from Sinopharm Chemical Reagent Co., Ltd. (Shanghai, China). Pt/C (20 wt% Pt on Vulcan XC-72R), Nafion (5 wt%) were purchased from Sigma-Aldrich Chemical Reagent Co., Ltd. Molybdenum mesh was purchased from Kangwei Metal wire Mesh Co., Ltd. All chemicals were used as received without further purification. Water used in all experiments was purified through a Millipore system (18.25 MΩ).

2.2. Synthesis of Mo@(2H-1T)-MoSe₂

Mo@(2H-1T)-MoSe₂ electrode materials were prepared by a facile in-situ hydrothermal etching method. First, the molybdenum mesh was sonicated in 3 M HCl aqueous solution, and the surface impurities were washed with water and ethanol. A certain amount of Na₂SeO₃ and 20 mL of deionized water was then added to a 50 mL Teflon-lined stainless steel autoclave with vigorous stirring for 30 min. Then the pretreated Mo mesh (1 × 4 cm²) was put into the autoclave and placed at an angle against the wall of the Teflon liner. Afterwards, the autoclave was sealed and then heated at 200 °C for 24 h. After being cooled down to room temperature, the sample was taken out, washed thoroughly with deionized water and ethanol, and then dried at 60 °C for 12 h under vacuum. The loading amount of MoSe₂ (2.82 mg cm⁻²) on Mo mesh was evaluated via inductively coupled plasma (ICP) analysis. A series of Mo@MoSe₂ were prepared with different concentrations of Na₂SeO₃ aqueous solution (0.15 mM, 0.3 mM, 0.6 mM, 0.9 mM, 1.2 mM, 1.5 mM, 1.8 mM) at different etching temperatures (100 °C, 150 °C, 200 °C, 250 °C) to verify the effect of concentration of Na₂SeO₃ and etching temperature on morphology, structure and the electrocatalytic properties. In addition, a series of Mo@MoSe₂ products were also synthesized in a 0.6 mM Na₂SeO₃ solution at 200 °C for expected reaction time (4 h, 10 h, 16 h, 24 h, 30 h, 36 h, 42 h, 48 h) to investigate the influence of reaction time on shape, structure and electrocatalytic properties. The preparation method of the comparison samples (Pt/C electrode and Mo-MoSe₂ electrode) is displayed in the [Supporting material](#).

2.3. Characterization

All samples were characterized by X-ray powder diffraction (XRD) on a Bruker D8 Advance X-ray powder diffractometer with Cu Kα radiation (λ = 1.5406 Å), scanning electron microscopy (SEM) on a JEOL JSM-7610F electron microscope, (high-resolution) transmission electron microscopy((HR)TEM) using JEOL F200 electron microscope with energy-dispersive X-ray microanalysis system. The X-ray photoelectron spectroscopy (XPS) analysis was measured on an X-ray photoelectron spectrometer (Thermo, ESCALAB 250XI and SHIMADZU-KRATOS, AXIS SUPRA) using Mg-Kα radiation. Raman spectroscopy was measured on the HORIBA LabRAM HR 800 with a 514 nm laser. Atomic force microscopy was performed on an Ara-Research Multimode AFM and operated in non-contact mode.

2.4. Electrochemical measurement

The HER performance was evaluated on an electrochemical workstation (Admiral instruments, Squidstat Plus, US) via a three-electrode system. The Mo@MoSe₂, Mo-MoSe₂, Pt/C and Mo mesh can be used directly as the working electrode with dimensions of 1 × 1 cm², using a graphite rod as the counter electrode. The saturated calomel electrode (SCE) was used as the reference electrode in phosphate buffer solution (PBS) and H₂SO₄, using Hg/HgO electrode as the reference electrode in KOH and natural seawater. Polarization curves were recorded by using linear sweep voltammetry (LSV) in various electrolyte solution with a scan rate of 2 mV s⁻¹. All potentials were calibrated with respect to the reversible hydrogen electrode (RHE) via the following equation: E_{RHE} = E_{Hg/HgO} + 0.059 pH + 0.098 V and E_{RHE} = E_{SCE} + 0.059 pH + 0.242 V. All the potentials in the LSV polarization curves were iR-corrected with respect to the ohmic resistance of the solution, unless specifically indicated. The electrochemical impedance spectroscopy (EIS) was performed with working electrode at open circuit potential with an ac perturbation of 5 mV while sweeping the frequency from 100 kHz to 0.01 Hz. The impedance data were fitted to a simplified Randles circuit to extract the series resistances (R_s) and charge-transfer resistances (R_{ct}). The stability test was carried out using chronopotentiometric measurements. The electrochemical surface area for working electrode was measured at various scan rates. The theoretical amount of H₂ evolved was then calculated by applying the Faraday law, which states that the passage of 96,485 C charge causes 1 equivalent of reaction.

The electrolyte of electrochemical test was 1 M phosphate buffer solution (pH = 7.01), 1 M KOH (pH = 13.6), 0.5 H₂SO₄ solution (pH = 0.4) and natural seawater (pH = 8.26). Natural seawater was collected from the Bohai Sea (Dalian, China), which was filtered to remove visible impurities before use.

2.5. Theoretical calculation

Spin-polarized DFT computations were performed via Vienna ab initio simulation package (VASP). The generalized gradient approximation (GGA) with PBE functional was used for the differential charge density. A plane-wave cutoff energy of 420 eV was used in all computations. A 2 × 2 supercell, three layers of pristine Mo (110) and monolayer of MoSe₂ (001) surface were chosen to construct the investigated models. Brillouin zone with 16 × 16 × 16 k-point was selected for geometry optimization. A vacuum region of around 15 Å was adopted to avoid interaction periodic images. The systems were relaxed until the energy and force reaching the convergence threshold of 5 × 10⁻⁵ eV and 0.05 eV/Å, respectively.

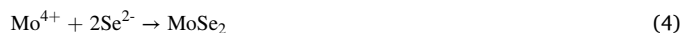
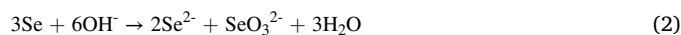
2.6. Piezo-catalytic RhB degradation in the dark with or without ultrasound

The degradation process of Rhodamine B (RhB) dye was performed in a sonicator with 40 KHz ultrasonic wave in the dark. Catalyst Mo@ (2H-1T)-MoSe₂ with 1 cm × 2 cm was put into 50 mL of aqueous solution of RhB dye (10 ppm) and kept for 5 s in the dark to ensure the catalyst was immersed in the RhB solution. Afterwards, the RhB solution with catalyst was sonicated in the dark for 10 s, 20 s, 30 s, 40 s, 50 s, 60 s, 120 s, 180 s, 300 s, 420 s, 540 s and 600 s to take 2 mL solution. After centrifugation, the supernatant was used to investigate the degradation activity of catalyst for RhB dye using a Purkinje General (China) T6 UV/Vis spectrophotometer and the visible-light absorbance of RhB was determined through its maximum absorption band at 553 nm to monitor the piezo-catalytic degradation efficiency. As a comparison, RhB degradation in the dark without ultrasound was also carried out under an identical condition.

3. Results and discussion

3.1. Morphology and structure of Mo@MoSe₂

As shown in Fig. 1, Mo@MoSe₂ monolithic electrode was synthesized by hydrothermal in-situ etching method. In short, using Na₂SeO₃ as the etchant and Mo mesh as the substrate, MoSe₂ is in-situ formed on the surface of Mo mesh by hydrothermal in-situ etching. SEM images of the cross section of Mo@MoSe₂ prepared by treating a clear Mo mesh in 0.6 mM Na₂SeO₃ solution at 200 °C for 16 h shown in Fig. S1a and b clearly indicate bark-like convex and concave surface structure, revealing in-situ growth of MoSe₂ architecture layer on Mo mesh surface. Energy disperse X-ray (EDX) line scanning profiles of Mo@MoSe₂ (Fig. S1c, d) reveal that MoSe₂ contents located at the convex area are much higher than those at concave area, further verifying in-situ growth mechanism of MoSe₂ on Mo surface. This result implies that metallic Mo is still dominated in the Mo@MoSe₂, and the inner crack areas have abundant active sites, which cannot be completely covered by in-situ formed MoSe₂ in the upper surface area [35]. The characteristic convex-concave structure can efficiently increase the accessible of surface area and the active sites. For the formation of Mo@MoSe₂, a detailed mechanism is elucidated as follows: Na₂SeO₃ as a strong base and weak acid salt shows weak alkalinity in solution (pH = 9.5). SeO₃²⁻ can be reduced to Se under heating conditions (Eq. (1)), and the newly formed Se will be further transformed into Se²⁻ through a disproportionation reaction (Eq. (2)) [36]. Meanwhile, Mo will be oxidized by oxygen dissolved in initial solution to form Mo⁴⁺ or Mo⁶⁺ (Eq. (3)), which can further react with Se²⁻ in solution to form MoSe₂ (Eq. (4)).



To systematically investigate the influences of Na₂SeO₃ concentration, reaction temperature and time on crystalline phase and morphology of in-situ formed Mo@MoSe₂ during the hydrothermal etching process, a series of Mo@MoSe₂ electrode materials were prepared and the detailed synthetic conditions are listed in Table S1.

As shown in Fig. 2a, the XRD patterns of Mo@MoSe₂ prepared by only adjusting the concentrations of Na₂SeO₃ under the identical other conditions clearly indicate that the diffraction peaks are mainly indexed to the Mo mesh (JCPDS 17-0887) and no crystalline MoSe₂ can be detected under a low concentration of Na₂SeO₃ (0.15 mM), while with gradually increasing concentrations of Na₂SeO₃ (0.6–1.8 mM) crystalline MoSe₂ formed and the diffraction peak appeared at 14.0° can be assigned to MoSe₂ (JCPDS 29-0914) except from the characteristic diffraction peaks of Mo, revealing that the increasing concentration of Na₂SeO₃ can efficiently promote the formation of crystalline MoSe₂ on Mo mesh, showing a characteristic concentration effect.

Additionally, by varying etching temperature from 100 °C to 250 °C and time from 4 h to 48 h, a series of Mo@MoSe₂ materials were obtained (Table S1). The XRD patterns in Fig. S2 verify the formation of MoSe₂, but the patterns are difficult to prove the phase transition of MoSe₂ from 2H to 1T. The Raman spectroscopy and XPS were employed to corroborate the formation and phase transition process of 2H-MoSe₂ and 1T-MoSe₂ in the Mo@MoSe₂ samples during the hydrothermal etching, due to that the characteristic Raman peaks A_{1g} (out-of-plane) and E_{2g}¹ (in-plane) of 2H-MoSe₂ appeared at 237.0 and 286.6 cm⁻¹, respectively (Fig. 2b) [37]. With increasing etching temperature, extra J₃ and J₄ peaks of 1T-MoSe₂ appeared at 197.6, 354.3 and 489.4 cm⁻¹, respectively, indicating phase transition from 2H-MoSe₂ to (2H-1T)-MoSe₂ [14]. Note that the intensity of the A_{1g} and E_{2g}¹ peak significantly decreased with the occurrence of phase transition in

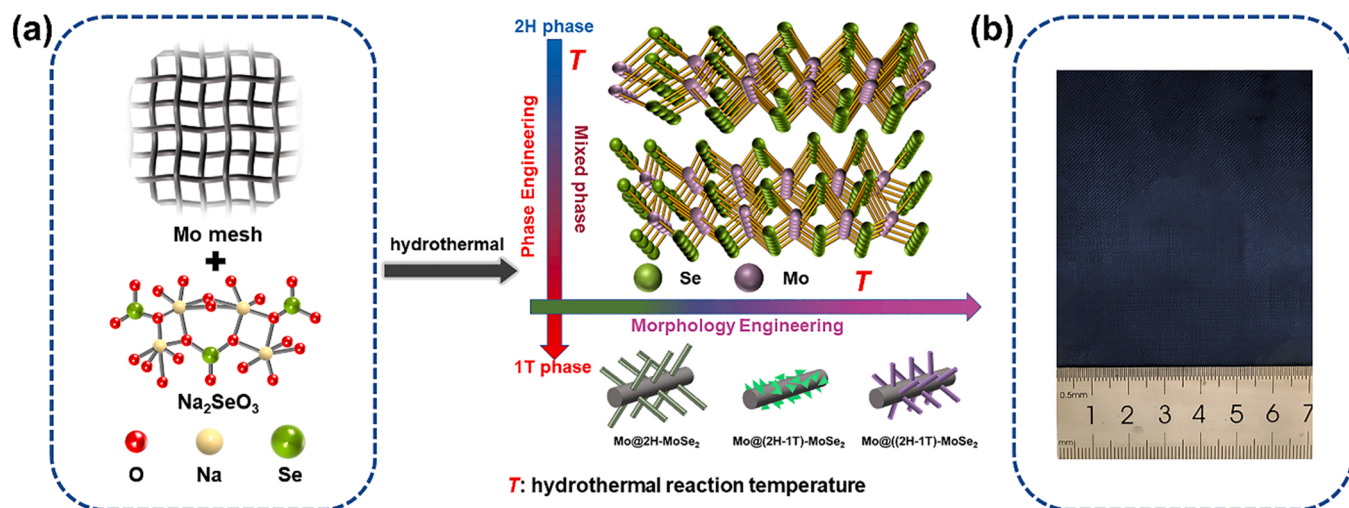


Fig. 1. (a) Schematic diagram of phase and morphology-controlled synthesis of MoSe₂ via hydrothermal in-situ etching of Mo mesh in Na₂SeO₃ solution, (b) photograph of the as-prepared Mo@2H-1T-MoSe₂ catalyst with dimensions of 7 × 8 cm².

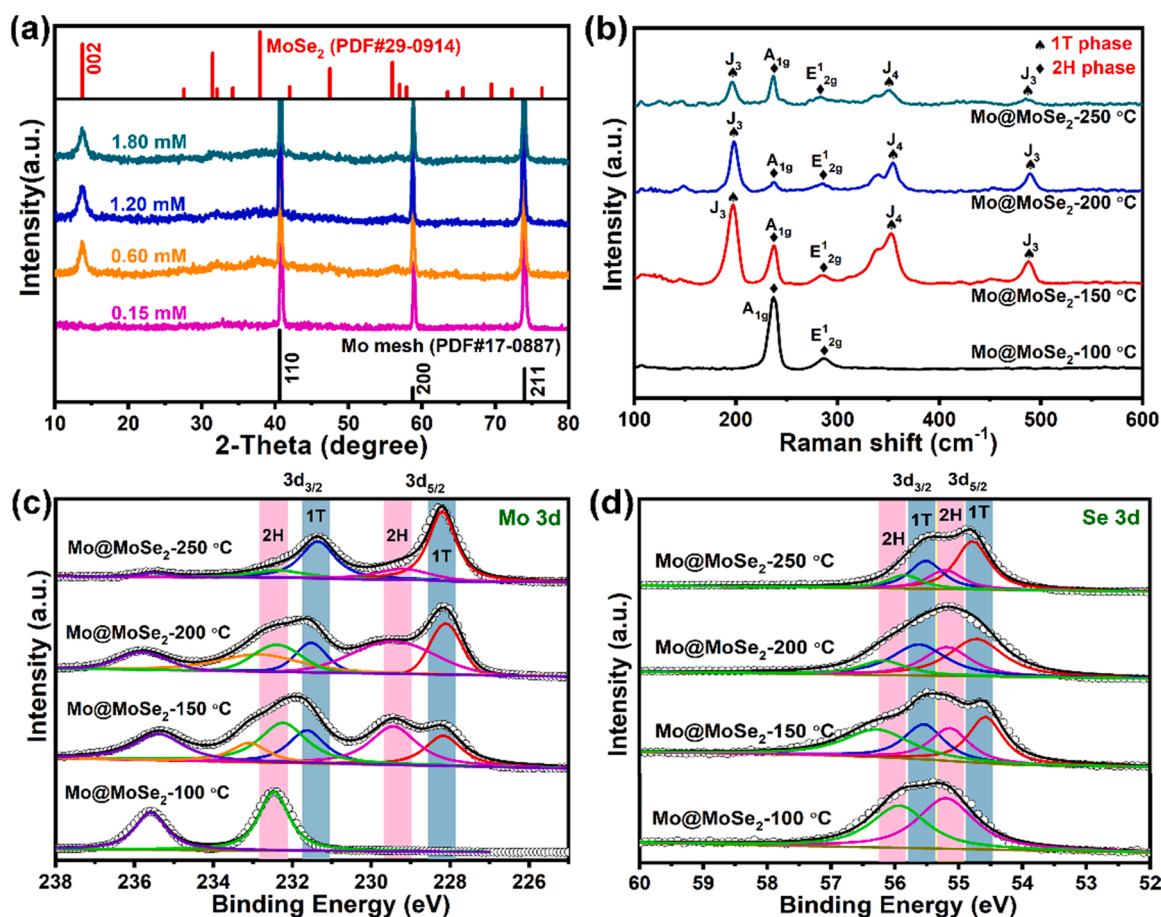


Fig. 2. (a) XRD patterns of Mo@MoSe₂ prepared by the etching of Mo mesh at 200 °C for 24 h under different concentrations of Na₂SeO₃, (b) Raman spectra of the Mo@MoSe₂ prepared at different reaction temperatures, and the high-resolution XPS spectra of Mo@MoSe₂ prepared at different reaction temperatures (c) Mo 3d and (d) Se 3d.

Mo@MoSe₂ composite. Based on characteristic Raman spectra of 1T phase of MoSe₂ [14,38], with increasing reaction temperature, the peak intensity ascribed to the 2H-MoSe₂ phase in the present Mo@MoSe₂ is relatively weakened, while the Raman intensity of the 1T phase is remarkably reinforced, especially for Mo@MoSe₂-200 °C, revealing the coexistence of 2H and 1T-MoSe₂. In addition, the coexistence of 2H and

1T-MoSe₂ in Mo@MoSe₂ can be further verified by XPS.

To further confirm the phase transformation of MoSe₂ with increasing etching temperature, the XPS spectra of Mo 3d and Se 3d are shown in Figs. 2c, d and S3. When Mo mesh was etched at 100 °C for 24 h, XPS spectrum of Mo 3d of Mo@MoSe₂ obtained indicates two peaks at 232.5 and 235.5 eV, which correspond to 2H phase of MoSe₂

and Mo^{6+} (the slight oxidation of MoSe_2 or Mo mesh surface exposed to air) [39], respectively, but 1T phase of MoSe_2 is not observed. When etching temperature was further increased to 150 °C, 200 °C and 250 °C, XPS spectra of Mo 3d show a series of peaks, which can be deconvoluted into four peaks at 228.1 and 231.4 eV, and 229.3 eV and 232.4 eV, in which the first two peaks are contributed to the binding energy of Mo 3d_{5/2} and 3d_{3/2} from 1T phase of MoSe_2 , and the last two peaks belong to Mo 3d_{5/2} and 3d_{3/2} from 2H phase of MoSe_2 , indicating the coexistence of 1T and 2H phase of MoSe_2 [7,37]. Note that the peak intensity of Mo 3d from 2H phase of MoSe_2 gradually decreased to 7% and that of 1T MoSe_2 correspondingly increased to 93% with elevating etching temperature from 100 °C to 250 °C (Table S2), clearly verifying the phase transition from 2H to 1T MoSe_2 . In addition, two weak peaks at 233.1 eV and 235.5 eV assigned to Mo 3d from MoO_3 still remain and gradually weaken. Furthermore, high-resolution XPS spectrum of Se 3d of Mo@MoSe_2 obtained at 100 °C only shows double peaks at 55.1 eV and 56 eV attributed to the 2H form of Se^{2-} (Fig. 2d), suggesting the existence of single phase 2H- MoSe_2 . When the etching temperature increases to 150 °C, 200 °C, 250 °C, the Se 3d spectra show two new peaks at 54.6 eV and 55.6 eV corresponding to the 1T phase of MoSe_2 , while two peaks originate from the 2H phase of Se^{2-} still preserve but the intensity gradually weaken [37]. On the basis of the results of XPS spectra of Mo 3d and Se 3d, 1T phase of MoSe_2 in Mo@MoSe_2 composite gradually increased and 2H- MoSe_2 correspondingly decreased with increasing etching temperature, indicating phase transition of MoSe_2 from 2H to 1T and the formation of mixed phase.

To further investigate etching temperature-driven the evolution of morphology and structure of Mo@MoSe_2 , Fig. 3 shows SEM and TEM images of Mo@MoSe_2 prepared at different etching temperatures. As shown in Fig. 3a and d, MoSe_2 nanorods with a diameter of about 50 nm were grown in the grooves of the bark at the etching temperature of 100 °C. When the temperature increases to 200 °C, the MoSe_2 nanosheets were arranged on Mo mesh (Fig. 3b, e). The thickness of MoSe_2 layer on Mo mesh is about 6.4 nm, as unveiled by AFM (Fig. S4). Such thickness of layer of hybrid 2H and 1T phase MoSe_2 nanosheets had a stronger the piezo-flexoelectric coupling effect at interfacial areas between 1T and 2H-phase, which has been confirmed by theoretical calculation and the improved electrocatalytic HER performance from previous reports [8,9]. This few-layered MoSe_2 nanosheets is conducive to the enhancement of HER activity in present work. With further elevating etching temperature to 250 °C, MoSe_2 nanotubes formed on Mo mesh showed a diameter of about 200 nm (Fig. 3c, f). For all Mo@MoSe_2 samples, HRTEM images (Fig. 3g–i) clearly show the interlayer lattice distance of 0.24 nm assigned to the diffraction (110) plane of Mo mesh. For Mo@MoSe_2 synthesized at 100 °C, the lattice fringes of 0.64 nm were observed anywhere (Fig. 3g), which is consistent with the interlayer spacing of (002) plane of 2H- MoSe_2 [7,38]. As temperature increases to 200 °C and 250 °C, the observed interlayer lattice distance is around 0.67 nm, which is indexed to (002) lattice plane of (2H-1T)- MoSe_2 nanosheets thanks to the coexistence of 1T and 2H phases (Fig. 3h, i) [7,37,40]. In addition, as a representative, EDX elemental mappings (Fig. 3j–l) of Mo@MoSe_2 prepared at 200 °C for 24 h demonstrate the existence and uniform distribution of elements Mo and Se in Mo@MoSe_2 . Based on above-mentioned results, the elevated hydrothermal etching temperature markedly induced the evolution of morphology of in-situ formed MoSe_2 on Mo mesh from nanorod to nanosheet, finally to nanotube and the corresponding phase transition from 2H phase to the mixed 2H-1T form of MoSe_2 , revealing a controllable morphology and phase engineering. The formation of mixed phase of MoSe_2 on Mo mesh and heterojunction structure among Mo and MoSe_2 as well as morphology evolution can efficiently change electrochemical activity and improve HER performance.

In addition, by changing the hydrothermal etching time from 4 h to 48 h, a series of Mo@MoSe_2 were successfully fabricated (Table S1, Fig. S2, no further discussion herein). For all Mo@MoSe_2 prepared at different Na_2SeO_3 concentrations, hydrothermal etching temperature

and time, their HER activities were investigated under the acidic, alkaline, neutral electrolyte media and in seawater environment to screen an optimal hydrothermal etching condition. The results from HER tests in Fig. S5 clearly reveal that the optimal hydrothermal etching conditions are that a clear Mo mesh was treated by using 0.6 mM Na_2SeO_3 solution at 200 °C for 24 h. To corroborate that the electrocatalytic performance of Mo@MoSe_2 stemmed from morphology effect or phase effect or their synergistic effect, the electrochemical impedance and electrochemical active area of Mo@MoSe_2 prepared at different temperatures were shown in Figs. S6–9 and S10. The Mo@MoSe_2 -200 °C exhibits a highest C_{dl} in 0.5 M H_2SO_4 , 1 M KOH, 1 M PBS and natural seawater compared with Mo@MoSe_2 -100 °C, Mo@MoSe_2 -150 °C and Mo@MoSe_2 -250 °C (Figs. S6–9), revealing the highly effective active sites of Mo@MoSe_2 -200 °C mainly induced by morphology effect. Furthermore, comparative study of among Mo@MoSe_2 -100 °C, Mo@MoSe_2 -150 °C, Mo@MoSe_2 -200 °C and Mo@MoSe_2 -250 °C, especially, Mo@MoSe_2 -100 °C and Mo@MoSe_2 -250 °C, the contribution of phase effect isn't very obvious, further revealing the dominant role of morphology effect. In addition, the results from the Nyquist plots suggest that the Mo@MoSe_2 -200 °C presents a similar R_s and an obviously different R_{ct} (Fig. S10). By using equivalent circuit shown in Fig. S11, the fitted resistances of EIS for catalysts Mo@MoSe_2 -100 °C, Mo@MoSe_2 -150 °C, Mo@MoSe_2 -200 °C and Mo@MoSe_2 -250 °C, are obtained and listed in Tables S3–6. A much smaller R_{ct} of Mo@MoSe_2 -200 °C in acidic, basic, neutral and natural seawater media implies a faster kinetics for HER compared to those of Mo@MoSe_2 -100 °C, Mo@MoSe_2 -150 °C and Mo@MoSe_2 -250 °C, further verifying high electrocatalytic performance of Mo@MoSe_2 -200 °C for HER. In this case, the obtained mixed 2H and 1T phases of MoSe_2 on Mo mesh was denoted as $\text{Mo@}(2\text{H}-1\text{T})\text{-MoSe}_2$. Due to the heterostructure, the piezo-flexoelectric coupling effect at interfacial areas between 1T and 2H-phase and nanosheet shape of MoSe_2 in $\text{Mo@}(2\text{H}-1\text{T})\text{-MoSe}_2$, their synergistic effect can greatly improve HER performance. Hence, HER activities of $\text{Mo@}(2\text{H}-1\text{T})\text{-MoSe}_2$ electrode in all pH scale ranges and seawater are investigated in detail as follows and compare to electrocatalysts Mo mesh, Mo- MoSe_2 and Pt/C. For the preparation of Mo- MoSe_2 electrode, a detailed procedure is described in the Supporting information.

3.2. HER performances of $\text{Mo@}(2\text{H}-1\text{T})\text{-MoSe}_2$ in all pH scale ranges and seawater

Fig. 4(a, d, g) shows LSV curves of electrocatalysts (Mo mesh, Mo- MoSe_2 , $\text{Mo@}(2\text{H}-1\text{T})\text{-MoSe}_2$ and Pt/C) in 0.5 M H_2SO_4 , 1 M KOH and 1 M PBS, respectively. In compared with blank Mo mesh and Mo- MoSe_2 , $\text{Mo@}(2\text{H}-1\text{T})\text{-MoSe}_2$ exhibits excellent electrocatalytic activities for HER, but the catalytic performances are inferior to that of commercial Pt/C (Fig. S12). The overpotentials of $\text{Mo@}(2\text{H}-1\text{T})\text{-MoSe}_2$ at 20 mA cm^{-2} are 183, 244, and 263 mV at 0.5 M H_2SO_4 , 1 M KOH and 1 M PBS, respectively. The corresponding Tafel slopes of $\text{Mo@}(2\text{H}-1\text{T})\text{-MoSe}_2$ derived from Fig. 4(a, d, g) are 72, 80, and 89 mV dec^{-1} in 0.5 M H_2SO_4 , 1 M KOH and 1 M PBS (Fig. 4b, e, h), indicating that the present results are in good agreement with that the small Tafel slope possessed a faster HER kinetics. In addition, by comparing LSV curves for HER of $\text{Mo@}(2\text{H}-1\text{T})\text{-MoSe}_2$ obtained in 0.5 H_2SO_4 , 1 M KOH and 1 M PBS (Fig. S13), the HER performance is similar only at the initial potential, and the performance in neutral solution will become inferior than that in alkaline solution with increasing applied voltages. The electrocatalytic activities of $\text{Mo@}(2\text{H}-1\text{T})\text{-MoSe}_2$ increase with an order in acidic > basic > neutral media, which does not maintain similar properties over all pH scale ranges. EIS was tested to investigate electrochemical reaction kinetics during the HER process. The semicircles shown in Nyquist plots of Mo mesh, Mo- MoSe_2 and $\text{Mo@}(2\text{H}-1\text{T})\text{-MoSe}_2$ (Fig. S14) indicate the charge transfer resistance (R_{ct}) of H^+ reaction between electrode and electrolyte [40]. Based on equivalent circuit shown in Fig. S11, the fitted resistances of EIS for three catalysts Mo mesh, Mo- MoSe_2 and $\text{Mo@}(2\text{H}-1\text{T})\text{-MoSe}_2$ in H_2SO_4 , KOH and PBS are

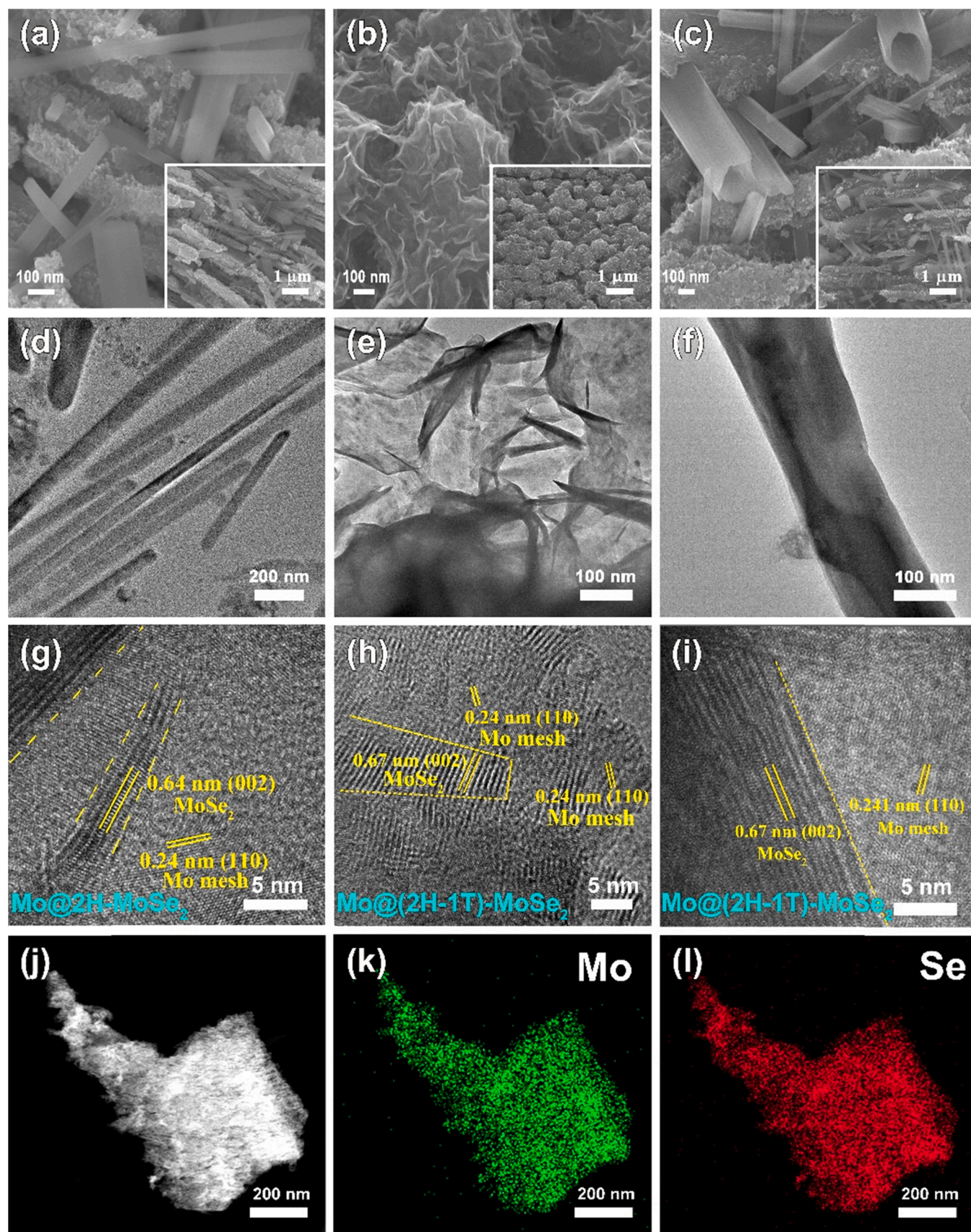


Fig. 3. Representative SEM, TEM and HRTEM images of Mo@MoSe₂ prepared at (a, d, g) 100 °C, (b, e, h) 200 °C, (c, f, i) 250 °C, (j) HAADF-STEM image of Mo@MoSe₂ prepared at 200 °C for 24 h and the corresponding EDX elemental mappings (k) Mo, and (l) Se.

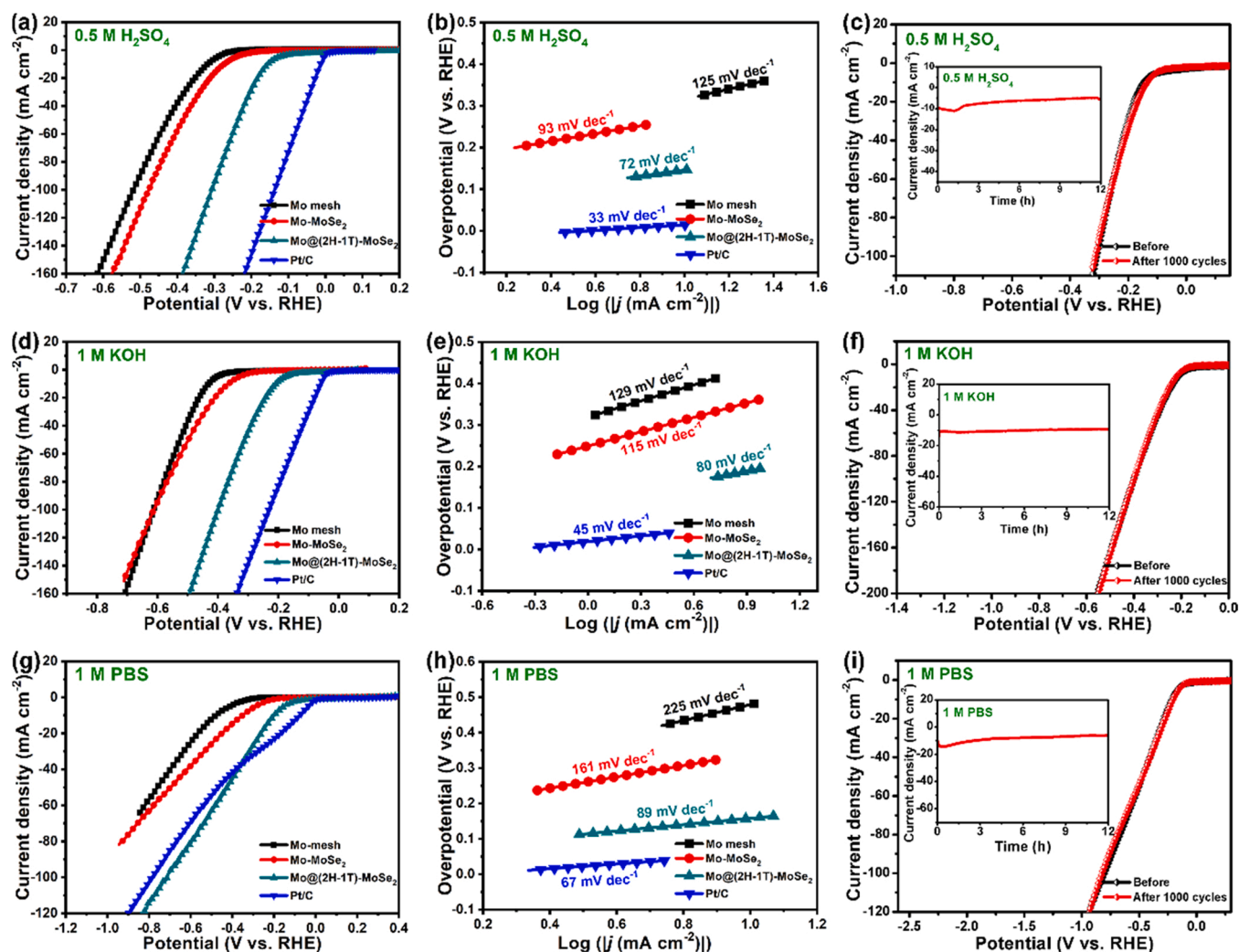


Fig. 4. HER performances of the electrocatalysts Mo mesh, Mo-MoSe₂, Mo@2H-1T-MoSe₂ and Pt/C in 0.5 M H₂SO₄, 1 M KOH and 1 M PBS, (a, d, g) LSV curves, (b, e, h) HER Tafel slopes derived from (a, d and g), and (c, f, i) LSV curves of Mo@2H-1T-MoSe₂ before and after 1000 CV cycles and the inset shows the stability test of electrocatalyst Mo@2H-1T-MoSe₂ for 12 h.

listed in Tables S7–9, respectively. It is obvious to find that all catalysts present a similar solution resistance (R_s) and completely different charge transfer resistance (R_{ct}). For all catalysts a clear semicircle is observed and the radius of arc markedly decrease with an order of Mo@2H-1T-MoSe₂ < Mo-MoSe₂ < Mo mesh in acidic, basic and neutral media, suggesting that a much smaller charge transfer resistance (R_{ct}) of Mo@2H-1T-MoSe₂ in different electrolytes reveals a more rapid electron transfer, implying a faster kinetics for HER and an improved HER performance [41,42]. We knew that the HER process mainly involves hydrogen atom adsorption reaction and following formation and release of H₂. 1T phase of MoSe₂ in Mo@2H-1T-MoSe₂ is conducive to the improvement of HER performance due to that the kinetic energy barrier of two hydrogen atoms adsorbed on the 1T-MoSe₂ to transform into a H₂ molecule is lower than that on 2H phase of MoSe₂ [40]. Such faster electron transfer in Mo@2H-1T-MoSe₂ is caused by the synergistic effect of 2H-1T phase of MoSe₂ (piezo-flexoelectric coupling effect) and heterostructure as the previously reported (1T-2H)-MoSe₂ [9], the heterostructural electrodes (2H, 1T)MoSe₂-La_{0.5}Sr_{0.5}CoO_{3-δ} and SWCNTs/graphene-MoSe₂ [43,44]. To further deeply understand the improved HER performance of Mo@2H-1T-MoSe₂, the effective electrochemical active surface areas (ECSA) of all catalysts were estimated by measuring the double-layer capacitance (C_{dl}) based on the CV results at different scan rates (Figs. S15–17) in different electrolytes (0.5 M H₂SO₄, 1 M KOH and 1 M PBS). The results indicate that the

ECSA of Mo@2H-1T-MoSe₂ electrode is 70.2 mF cm⁻² in 0.5 M H₂SO₄ solution, 91.5 mF cm⁻² in 1 M KOH solution and 33.1 mF cm⁻² in 1 M PBS solution, which is higher than those of electrodes Mo mesh and Mo-MoSe₂ in acidic, basic and neutral media under an identical condition, revealing that the piezo-flexoelectric coupling effect in-situ formed 2H and 1T phases of MoSe₂ on Mo mesh and the heterojunction interfaces among Mo, 2H and 1T forms of MoSe₂ can efficiently enhance the electrochemical active area and drive more exposed active sites (concave-convex bark-like surface structure) for HER process [7,9,13]. The turnover frequency (TOF, the amount of H₂ molecules produced from one active site per second) was used to study the intrinsic activity of the catalyst [45]. The calculated TOF values of Mo@2H-1T-MoSe₂ and Mo-MoSe₂ in alkaline solution are 8.6533×10^{-4} H₂/s and 2.7454×10^{-4} H₂/s at -0.10 V, respectively, indicating highly intrinsic catalytic activity of the Mo@2H-1T-MoSe₂ (Table S11). In addition, to investigate the electrochemical stability and cycle durability of the Mo@2H-1T-MoSe₂, the continuous sweep voltammetry of 1000 cycles was conducted in 0.5 M H₂SO₄, 1 M KOH, and 1 M PBS solution, respectively (Fig. 4c, f, i). The results showed the same LSV curves as before, confirming high electrochemical stability and cycle durability. The chronoamperometry tests demonstrate that Mo@2H-1T-MoSe₂ shows neglectable decay over 12 h. The multi-potential and multi-current steps tests (Fig. S18) keep a constant under different potentials and currents, further demonstrating the high durability of Mo@2H-1T-MoSe₂.

electrode. Furthermore, SEM images of Mo@ (2H-1T)-MoSe₂ after 12 h-HER tests manifest the preservation of the original morphology of Mo@ (2H-1T)-MoSe₂ in 1 M KOH and 1 M PBS, and a slight alteration of morphology in 0.5 M H₂SO₄ (Fig. S19). The XPS spectra of Mo@ (2H-1T)-MoSe₂ before and after HER tests for 12 h in different electrolyte shown in Figs. S20–23 display that high-resolution XPS of Mo 3d of the Mo@ (2H-1T)-MoSe₂ could be deconvoluted to 228.1 and 231.4 eV assignable to 1T phase of MoSe₂, and 229.3 and 232.4 eV attributable to 2H phase of MoSe₂, respectively. Nevertheless, after HER test, the intensities of peaks corresponding to 1T and 2H phase obviously decreased, while the peaks at 233.1 and 236.0 eV ascribable to Mo⁶⁺ significantly increased, showing the partial oxidation of MoSe₂ or Mo surface [39]. In addition, the Se 3d core level spectrum of Mo@ (2H-1T)-MoSe₂ show two doublets of 1T phase at 54.6 and 55.6 eV, and 2H phase at 55.1 and 56.0 eV, respectively.

In order to further explore the enhanced HER activity mechanism, operando EIS technique was employed in different electrolytes. As shown in Figs. S24–26(a, b), the Nyquist plots of Mo@ (2H-1T)-MoSe₂ and Mo-MoSe₂ were collected in different electrolytes (0.5 M H₂SO₄, 1 M KOH and 1 M PBS) at various applied potentials. It is obvious that the semicircles for Mo-MoSe₂ and Mo@ (2H-1T)-MoSe₂ markedly decreased with increasing potentials, but radius of arcs for Mo@ (2H-1T)-MoSe₂ are much less than those from Mo-MoSe₂ in different electrolytes, indicating that Mo@ (2H-1T)-MoSe₂ has smaller resistance. Combined with the corresponding the Bode phase plots, which can reveal the trend of phase angle variation with the change of frequency, the Bode diagram is described as in the high-frequency region and in the low-frequency region. The signals in the high and low frequency regions are attributed to the electronic conduction in the inner-layer/interface of the catalyst and the reaction charge transfer at the electrolyte-catalyst interface, respectively [46]. As shown in Fig. S24(c, d), for MoSe₂-based catalysts, the Bode plots can be divided into the low and high frequency areas. Under an acidic solution, with increasing applied potential, Mo-MoSe₂ and Mo@ (2H-1T)-MoSe₂ have the different behaviors in the two frequency regions. For Mo-MoSe₂ electrode, with increasing potential, the phase angle in low frequency area gradually decreased and moved to the high frequency direction, implying that the HER resistance originated from both the electrolyte-catalyst interface charge transfer resistance and electron transfer resistance evolved the dominant electron transfer resistance. Although the phase angle variation of Mo@ (2H-1T)-MoSe₂ electrode has a similar trend as Mo-MoSe₂, the phase angle in high frequency area quickly decreased and the phase angle is lower than that of Mo-MoSe₂ at same frequency and same applied potential, implying a rapid inner-layer/interface electron transfer ability of Mo@ (2H-1T)-MoSe₂ electrode and a fast HER kinetics. The rapid transfer of electron in the internal electric fields created piezoelectric potential [8,9], while the local defect sites, cracking edge active site and the structural boundaries between the 1T and 2H phases of MoSe₂ nanosheets induced flexoelectric potential [9]. In addition, the formation of heterojunctions among Mo, 2H, 1T MoSe₂ also accelerated electron transfer. Hence the piezo-flexoelectric coupling effect and heterojunction effect in Mo@ (2H-1T)-MoSe₂ electrode are responsible for rapid electron transfer ability of electrode and fast HER kinetics. Note that, under an identical applied potential, the influence of the electrolyte-catalyst interface charge transfer resistance for Mo@ (2H-1T)-MoSe₂-catalyzed HER is weaker than that from Mo-MoSe₂, and the effect of the inner-layer/interface electron transfer resistance from Mo-MoSe₂ for HER is stronger than that from Mo@ (2H-1T)-MoSe₂ compared to Fig. S24c and d. However, under a basic condition (1 M KOH solution), for Mo-MoSe₂, with increasing potential, the roles of both from the electrolyte-catalyst interface charge transfer and the catalyst inner-layer/interface electron transfer resistance changed in high and low frequency area for HER (Fig. S25c). For Mo@ (2H-1T)-MoSe₂, it is obvious to find that catalyst inner-layer/interface electron transfer resistance is a main factor to influence HER (Fig. S25d), indicating that the characteristic piezo-flexoelectric

coupling effect and heterojunction interface effect is beneficial to electron transfer during HER process. Furthermore, when a neutral electrolyte solution (1 M PBS) was used, with increasing potential, for Mo-MoSe₂ and Mo@ (2H-1T)-MoSe₂, the similar Bode phase plots in two frequency regions were observed as that under acidic condition (Fig. S26c, d). These results clearly confirm the differences of electron transfer resistance for the influence on HER in different electrolytes, further verifying the complexity of electrocatalysis. Noticeably, the response of phase angle of Mo-MoSe₂ and Mo@ (2H-1T)-MoSe₂ with applied voltages shown in Fig. S27 reveals that the response of Mo@ (2H-1T)-MoSe₂ is faster than Mo-MoSe₂ and displays a greater downward trend, implying a faster kinetics of Mo@ (2H-1T)-MoSe₂ and the presence of more electrons in HER. The fitted quantitative value for high and low frequency in the bode phase plots at different applied potentials are summarized in Tables S12–17. Therefore, smaller intrinsic resistance in Mo@ (2H-1T)-MoSe₂ is confirmed to promote the HER kinetics and the rate-limiting step involving the adsorption of H atoms and its conversion into H₂ depended on the intrinsic activity of Mo and Se active sites, and a rapid electron transfer stemmed from the phase and morphology engineering effects.

Seawater is considered to be a major hydrogen reservoir. In general, most electrocatalysts in seawater are easily corroded and exhibit low electron conductivity, and thereby lead to the weak activity and high instability [47]. At present, the rational design and successful preparation of robust and selective electrocatalysts are the key chemical challenges for splitting of seawater [48]. The development of electrocatalysts with high stability and catalytic performance for HER in seawater is a top priority. Herein, we use Mo@ (2H-1T)-MoSe₂ as a electrocatalyst to explore its catalytic activity for HER in seawater and compare with the results from the electrodes Mo mesh, Mo-MoSe₂ and Pt/C. As can be seen in Fig. 5a, for the electrodes Mo mesh, Mo-MoSe₂, Pt/C and Mo@ (2H-1T)-MoSe₂, LSV curves show that Pt/C has a lowest overpotential about 317 mV at the current density of 20 mA cm⁻², and the overpotential of 470 mV for Mo@ (2H-1T)-MoSe₂ is higher than that from Pt/C and much lower than those from Mo mesh (838 mV) and Mo-MoSe₂ (858 mV). The corresponding Tafel slope of the electrode Mo@ (2H-1T)-MoSe₂ is 196 mV dec⁻¹ (Fig. 5b), which is lower than those from Mo mesh (262 mV dec⁻¹) and Mo-MoSe₂ (250 mV dec⁻¹) but higher than that from electrode Pt/C (85 mV dec⁻¹), corroborating a high HER activity of Mo@ (2H-1T)-MoSe₂ in seawater. As seen in the Nyquist plots (Fig. S28), three catalysts present a similar R_s and an obviously different R_{ct}. By using equivalent circuit shown in Fig. S28, the fitted resistances of EIS for Mo mesh, Mo-MoSe₂ and Mo@ (2H-1T)-MoSe₂ catalysts are listed in Table S10. The Mo@ (2H-1T)-MoSe₂ possesses a much smaller R_{ct} than Mo mesh and Mo-MoSe₂, suggesting a faster kinetics for HER. To further explore catalytic activity of Mo@ (2H-1T)-MoSe₂ in HER and compare with Mo mesh and Mo-MoSe₂ in seawater, ECSA of three catalysts was estimated by measuring the C_{dl} based on the CV results at different scan rates (Fig. S29) in natural seawater. The results show that the ECSA of Mo@ (2H-1T)-MoSe₂ is 20.26 mF cm⁻² in seawater, which is higher than those of Mo mesh (9.42 mF cm⁻²) and Mo-MoSe₂ (10.30 mF cm⁻²), revealing that the effectively active sites of Mo@ (2H-1T)-MoSe₂ induced by heterojunction interface effect and morphology effect aren't blocked/deactivated. In addition, the results from the chronoamperometry and chronopotentiometry measurements suggest the good durability of the Mo@ (2H-1T)-MoSe₂ for HER in natural seawater (Fig. S30). Subsequently, the stability and durability of Mo@ (2H-1T)-MoSe₂ were further studied by comparison of its LSV curve before and after 1000 cycles (Fig. 5c). When current density was fixed at 100 mA cm⁻², the amount of evolved H₂ is in good agreement with the calculated value (Fig. 5f), indicating the Faradic efficiency of Mo@ (2H-1T)-MoSe₂ is about 100% for HER in seawater. The high durability of the electrode prevents the corrosion and poisoning from chemical and biological impurities in seawater.

Furthermore, operando EIS is also used to estimate the electrode

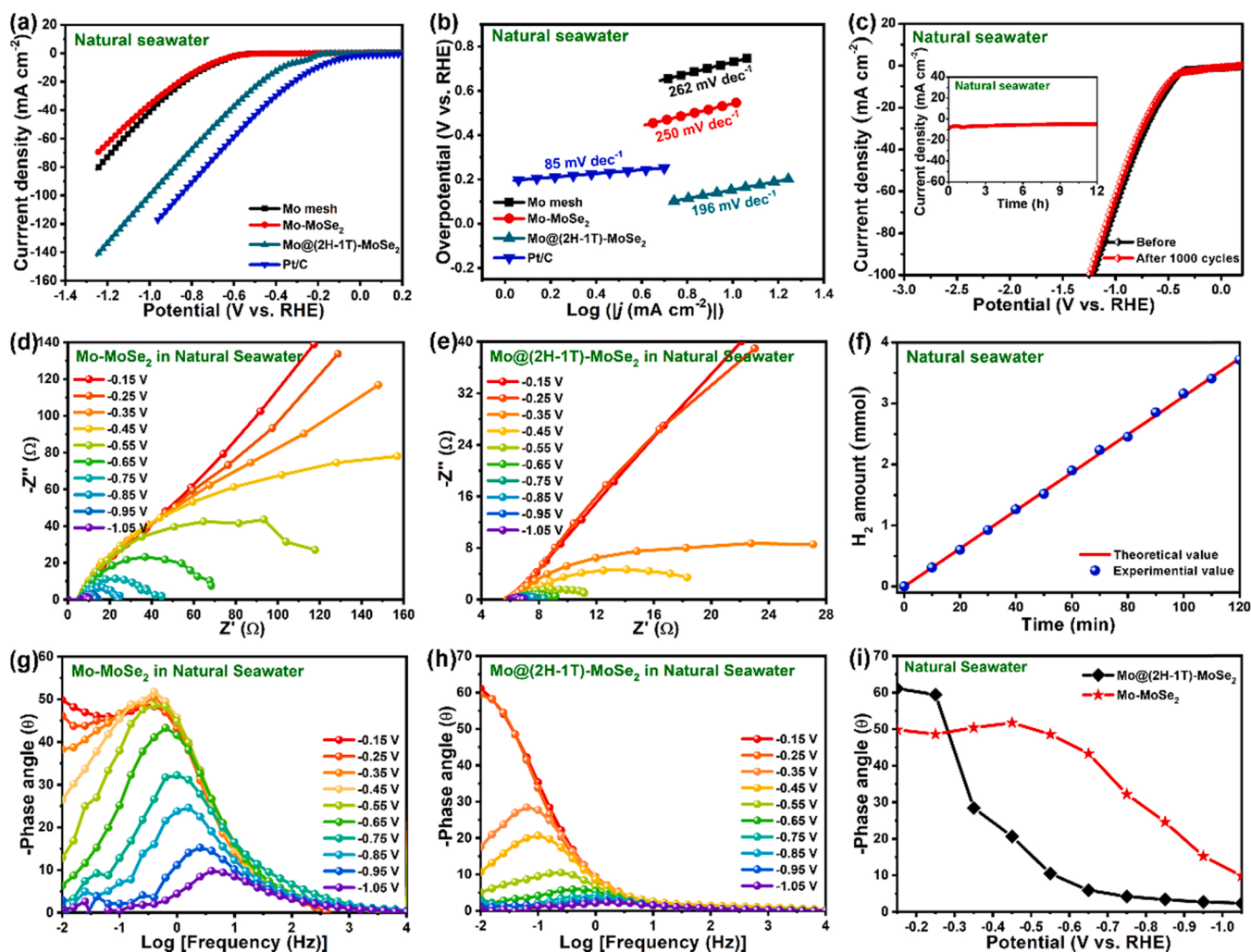


Fig. 5. (a) LSV curves and (b) the corresponding Tafel slopes for the electrodes Mo mesh, Mo-MoSe₂, Mo@2H-1T-MoSe₂ and Pt/C in natural seawater, (c) LSV curves for Mo@2H-1T-MoSe₂ before and after 1000 CV cycles, the inset shows the stability test for Mo@2H-1T-MoSe₂ after 12 h-HER test. Nyquist plots at different applied potentials in seawater for catalysts (d) Mo-MoSe₂ and (e) Mo@2H-1T-MoSe₂. (f) Detected and calculated H₂ amounts by the electrolyzer at a fixed current density of 100 mA cm⁻². The corresponding Bode phase plots at different applied potentials for catalysts (g) Mo-MoSe₂ and (h) Mo@2H-1T-MoSe₂. (i) Response of the phase angle to the applied potential of Mo-MoSe₂ and Mo@2H-1T-MoSe₂.

kinetics in natural seawater. As illustrated in Nyquist plots (Fig. 5d, e) of Mo-MoSe₂ and Mo@2H-1T-MoSe₂ at applied potentials from -0.7 to -1.6 V in seawater, when the applied potential reaches -0.90 V, the circle arcs of Mo@2H-1T-MoSe₂ decreases significantly, indicating a lower R_{ct} and a faster reaction kinetics. Comparing with Mo-MoSe₂, the phase angle of Mo@2H-1T-MoSe₂ in the medium and high frequency region is much smaller than that in the low frequency region, and the phase angle quickly decreased in high frequency area, implying that the inner-layer/interface electron transfer of catalyst is much faster than the electrolyte-catalyst interface charge transfer (Fig. 5g, h). The quantitative value fitted for Nyquist plots at different applied potentials in seawater are summarized in Tables S18, 19. From the response of the phase angle, the Mo@2H-1T-MoSe₂ displays a greater downward trend than Mo-MoSe₂ (Fig. 5i), further corroborating that the HER process of Mo@2H-1T-MoSe₂ still preserves a faster reaction kinetics in seawater, due to that the heterojunction structures among Mo, 2H-MoSe₂ and 1T-MoSe₂ and the piezo-flexoelectric coupling effect at the interfacial area between hybrid 2H and 1T MoSe₂ are conducive to electron transfer, and revealing an outstanding HER activity in seawater. On the basis of aforementioned investigations and results, a summary of comparatively electrocatalytic performance of MoSe₂-based electrodes is listed in Table S20 in acidic, basic and neutral media even in seawater,

clearly indicating that most MoSe₂-based electrocatalysts for HER mainly focused on the acidic condition and only a few samples were investigated in the basic media. A recent review on the phase modulation of molybdenum disulfide/diselenide and their applications in electrocatalysis also focused on the challenges in the acid, and the investigations in basic solution and seawater were almost neglected [49]. In this study, Mo@2H,1T-MoSe₂ indicated the excellent performances in all pH scale ranges and seawater, which is attributed to the synergistic effect derived from the piezo-flexoelectric coupling effect of 2H-1T phase of MoSe₂ and heterostructure effect between Mo and MoSe₂ as well as high stability and cycle durability.

Due to the simplicity and expandability of in situ etching method, a large-area Mo@2H-1T-MoSe₂ monolithic electrode with dimensions of 7×8 cm² can be synthesized (Fig. 1b). The HER test of the large-area electrode was performed in acidic, basic, neutral solution and seawater and the results are shown in Fig. S31, revealing an excellent HER performance. Furthermore, this facile and effective hydrothermal in-situ etching strategy can also be applied arbitrarily to the preparation of M@MSe_x (M = Ni, Cu, W etc.) with heterojunction structure by etching metal mesh in Na₂SeO₃ solution. The corresponding HER activities of as-made electrocatalysts are shown in Figs. S32 and S33, verifying an improved electrocatalytic performance compared to metal

substrate. Although the previous report also indicated that trimultiple-phase 3D trimetallic Mo-Ni-Co selenide nanorod array could be in-situ fabricated on a Ni-Co foam via the multiple-steps and complicate process [50]. Therefore, in the present work, a simple hydrothermal in-situ etching method paves a wide avenue for the large-scale preparation of electrocatalysts metal-metal selenide with heterostructure for the practical industrial application in HER and further in OER.

3.3. Density-functional theoretical calculation

The DFT calculations were further performed to profit deeply the insight of Mo-MoSe₂ heterostructure and reveal inherent mechanism of promoted HER activity. As shown in the differential charge density

(Fig. 6a), the electrons flowed from the MoSe₂ to the Mo mesh, which can not only accelerate the breaking of the H-OH bond but also adsorb the H_{ad} on the metallic Mo centers [35]. The electrostatic potentials of the Mo (110) surface and MoSe₂ (001) surface are shown in Fig. 6b, whereas the work functions of the Mo (110) surface and MoSe₂ (001) surface are 4.70 and 3.37 eV, respectively, implying that the electrons on MoSe₂ can transfer to Mo until the Fermi level equilibrium. According to the theory of semiconductor physics, a Mott-Schottky heterojunction of metallic Mo and N-type semiconductor MoSe₂ is achieved. To study the contact interface between Mo and MoSe₂, the energy band diagrams before and after contact are plotted in Fig. 6c. When the MoSe₂ connects with Mo, electrons flow from MoSe₂ to Mo, resulting in electrons redistribution. A large amount of negative charge accumulated on

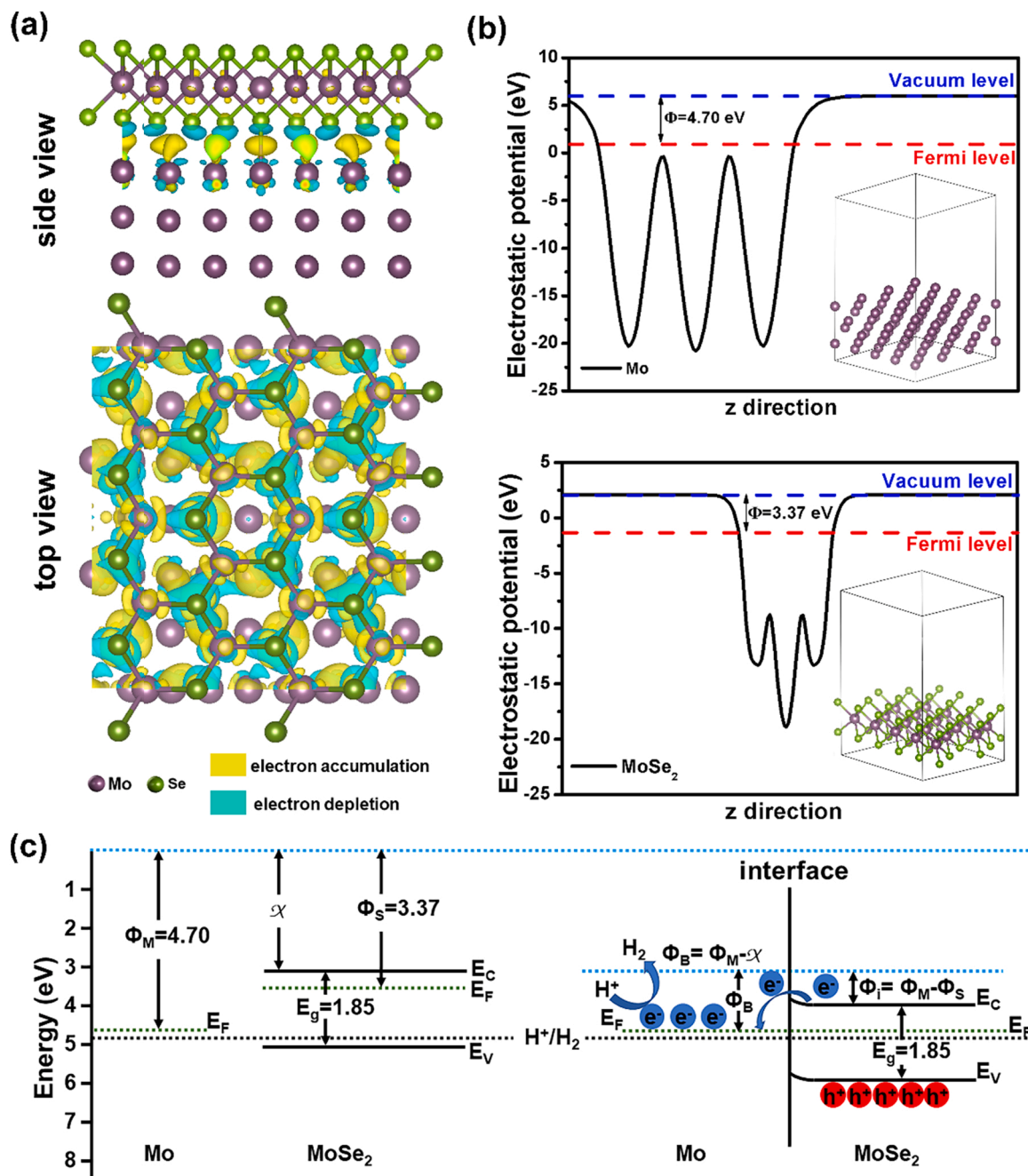


Fig. 6. Computational studies, (a) the charge density distribution at the interface of the Mo@MoSe₂ heterostructure, (b) the electrostatic potential calculations of Mo metal (top) and MoSe₂ (bottom), (c) the energy levels of the two components in Mo@MoSe₂ before and after contact. The black dash lines are the reduction potentials of HER.

the metal side, which is conducive to form the H_{ad} intermediates. Thus, the interfacial charge redistribution caused by the Mott-Schottky heterojunction could increase the intrinsic activity of electrocatalyst, and thereby promote HER performance. In addition, the piezo-flexocatalytic coupling effect of hybrid 1T and 2H-phase few-layered $MoSe_2$ nanosheets in HER has been confirmed from previous study [8,9].

Based on above-mentioned morphologies and structures of $Mo@MoSe_2$ prepared and HER results, the catalytic performance is very difficult to only contribute to the influence of certain single factor. Although the previous reports revealed that 1T phase of $MoSe_2$ indicated a highly catalytic activity for HER compared to that of 2H phase of $MoSe_2$ [7,14,37,38,40] implying that the catalytic activity for HER enhanced with increasing 1T phase content of $MoSe_2$ in composite, but in present work the electrode $Mo@(2H-1T)-MoSe_2-250$ with 93% 1T phase listed in Table S2 didn't show a highest catalytic performance, oppositely, $Mo@(2H-1T)-MoSe_2$ with 45% 1T phase and 55% 2H phase indicated a highest catalytic activity for HER. For all $Mo@MoSe_2$ catalysts prepared under various conditions (temperature, reaction time and concentration), they still contain Mo, 2H or mixed 2H-1T phase of $MoSe_2$ and heterojunctions of Mo- $MoSe_2$ and of 2H-1T phase of $MoSe_2$ as well as various morphologies. No matter how the phase and morphology of $MoSe_2$ change, the heterojunction between Mo and $MoSe_2$ still preserves. Hence, the morphology and 2H-1T phase content are acting as the vital roles to directly decide catalytic activity for HER. However, it is obvious to find that nanosheet-shaped $MoSe_2$ exhibited a highly activity compared to those of nanorods and nanotubes by HER results, consequently, the synergistic effect of 2H-1T phase of $MoSe_2$ nanosheets is becoming a focus to explain a highest catalytic activity of $Mo@(2H-1T)-MoSe_2$. On the basis of morphology and structure of $Mo@(2H-1T)-MoSe_2$ characterized by SEM and TEM images, and the combination of the thickness of few-layered $MoSe_2$ nanosheets about 6.4 nm with previous reports [8,9,31–34], piezo-/flexoelectrical potential effect is suggested to well explain the highest catalytic performance for HER. To confirm the existence of piezo/flexo-catalytic effect in $Mo@(2H-1T)-MoSe_2$, RhB degradation in the dark by $Mo@(2H-1T)-MoSe_2$ was performed with and without ultrasound. The degradation ratio of RhB catalyzed by $Mo@(2H-1T)-MoSe_2$ in the dark without ultrasound reached 33% within 10 min, but with ultrasound in the dark, the degradation ratio reached 82% (Fig. S34a–c), clearly revealing the efficient separation of electron and hole in the presence of the electron field as ultrasonic wave as mechanical stress was exerted on the $Mo@(2H-1T)-MoSe_2$ nanosheets and confirming the piezoelectricity and semiconductor property of $Mo@(2H-1T)-MoSe_2$ [8,9,31–34]. For $M@MSe_x$ ($M = Ni, Cu$), no piezo-catalytic effect can be observed for RhB degradation in the dark with and without ultrasound. In addition, the flexoelectricity potential of 2H-1T- $MoSe_2$ nanosheets induced by local defect sites, cracking edge-site defects, structural phase boundaries and strain gradient, which has been previously confirmed by theoretical calculation and HER experiment [9]. Due to that $Mo@(2H-1T)-MoSe_2$ in this work has a similar morphology and structure as well as thickness as that of reported hybrid 2H-1T $MoSe_2$ [9], this material possesses flexoelectricity. Finally, by DFT theoretical calculation, heterojunction effect of $Mo@(2H-1T)-MoSe_2$ was unveiled. Hence, the highest catalytic activity of $Mo@(2H-1T)-MoSe_2$ for HER can be contributed to the synergistic interaction of the piezo-flexoelectric coupling effect of hybrid 2H-1T phase of $MoSe_2$ nanosheets, few-layered nanosheet morphology and heterojunction effects.

4. Conclusions

In conclusion, a facile and effective hydrothermal in-situ etching strategy was developed to fabricate the heterostructure $MoSe_2$ on Mo mesh in Na_2SeO_3 aqueous solution. By adjusting Na_2SeO_3 concentration in system, $MoSe_2$ contents on Mo mesh can be well controlled. The elevated reaction temperature induced the consecutive phase transition from 2H form to the mixed 2H-1T phase in $MoSe_2$ verified by Raman

spectra and XPS, and the morphological evolution of $MoSe_2$ from nanorod to nanosheet and nanotube, while reaction time further optimized the electrocatalytic activity of obtained product. The high-quality heterojunction $Mo@(2H-1T)-MoSe_2$ electrocatalyst was successfully prepared under an optimal condition and used for HER in all pH scale ranges and seawater. Benefiting from the synergistic interaction of the piezo-flexoelectric coupling effect at interfacial areas between 1T and 2H-phase of $MoSe_2$ nanosheets with thickness of 6.4 nm and heterojunction interface between $MoSe_2$ layer and Mo mesh, $Mo@(2H-1T)-MoSe_2$ exhibits the excellent electrocatalytic activities for HER in all pH ranges and seawater, evidenced by LSV measurements and electrochemical reaction kinetics. In addition, Operando EIS and theoretical calculations revealed that the heterojunction interfaces among Mo, 2H and 1T phase of $MoSe_2$ in $Mo@(2H-1T)-MoSe_2$ fabricated via hydrothermal in-situ etching strategy are playing the pivotal roles for improved HER performance. Due to the simplicity and expandability of in situ etching method, this strategy can be extended arbitrarily to the preparation of the large-scale monolithic electrodes not only $Mo@MoSe_2$ but also other $M@MSe_x$ ($M = Ni, Cu, W$, etc.) with heterojunction interface, and indicate the high catalytic activity in HER. This study provides a simple, effective and low-cost approach to fabricate the state-of-the-art metal-based heterostructured electrocatalysts for potentially commercial application in (sea)water splitting.

CRediT authorship contribution statement

Chunming Yang: Conceptualization, Writing – review & editing. **Lihai Zhou:** Methodology, Data curation. **Chuantao Wang:** Conceptualization, Data curation, Validation. **Wen Duan:** Validation. **Le Zhang:** Data curation. **Fuchun Zhang:** Validation. **Junjun Zhang:** Validation. **Yanzhong Zhen:** Conceptualization, Resources. **Loujun Gao:** Conceptualization, Resources, Validation. **Feng Fu:** Project administration, Supervision, Funding acquisition. **Yucang Liang:** Conceptualization, Supervision, Writing – review & editing.

Declaration of Competing Interest

The authors declare that they have no known competing financial interests or personal relationships that could have appeared to influence the work reported in this paper.

Acknowledgments

This work was supported by National Natural Science Foundation of China (Grant Nos. 22162025, 21902123, 22068037), Natural Science Basic Research Plan in Shaanxi Province of China (2021JQ-612, 2021JQ-628), Natural Science Foundation of Shaanxi Provincial Department of Education (20JK0996), the Key Laboratory Foundation of Shaanxi Provincial Education Office of China (18JS115), Yan'an High-Level Talent Special Project, Talent Introduction Training Project (2019-20), Ph.D. research startup foundation of Yan'an University (YDBK2019-28, YDBK2019-29), and University-level scientific research project of Yan'an University (YDY2020-37, YDY2020-41).

Appendix A. Supplementary material

Supplementary data associated with this article can be found in the online version at doi:10.1016/j.apcatb.2021.120993.

References

- [1] I.S. Kwon, I.H. Kwak, T.T. Debela, H.G. Abbas, Y.C. Park, J.-p. Ahn, J. Park, H. S. Kang, Se-rich $MoSe_2$ nanosheets and their superior electrocatalytic performance for hydrogen evolution reaction, *ACS Nano* 14 (2020) 6295–6304, <https://doi.org/10.1021/acsnano.0c02593>.

- [2] I. Staffell, D. Scamman, A.V. Abad, P. Balcombe, P.E. Dodds, P. Ekins, N. Shah, K. R. Ward, The role of hydrogen and fuel cells in the global energy system, *Energy Environ. Sci.* 12 (2019) 463–491, <https://doi.org/10.1039/C8EE01157E>.
- [3] M. Yao, B. Wang, B. Sun, L. Luo, Y. Chen, J. Wang, N. Wang, S. Komarneni, X. Niu, W. Hu, Rational design of self-supported Cu@WC core-shell mesoporous nanowires for pH-universal hydrogen evolution reaction, *Appl. Catal. B Environ.* 280 (2021), 119451, <https://doi.org/10.1016/j.apcatb.2020.119451>.
- [4] X. Wu, S. Zhou, Z. Wang, J. Liu, W. Pei, P. Yang, J. Zhao, J. Qiu, Engineering multifunctional collaborative catalytic interface enabling efficient hydrogen evolution in all pH range and seawater, *Adv. Energy Mater.* 9 (2019), 1901333, <https://doi.org/10.1002/aenm.201901333>.
- [5] Y. Wang, G. Qian, Q. Xu, H. Zhang, F. Shen, L. Luo, S. Yin, Industrially promising IrNi-FeNi₃ hybrid nanosheets for overall water splitting catalysis at large current density, *Appl. Catal. B Environ.* 286 (2021), 119881, <https://doi.org/10.1016/j.apcatb.2021.119881>.
- [6] Y. Zhao, B. Jin, Y. Zheng, H. Jin, Y. Jiao, S.Z. Qiao, Charge state manipulation of cobalt selenide catalyst for overall seawater electrolysis, *Adv. Energy Mater.* 8 (2018), 1801926, <https://doi.org/10.1002/aenm.201801926>.
- [7] S. Deng, Y. Zhong, Y. Zeng, Y. Wang, Z. Yao, F. Yang, S. Lin, X. Wang, X. Lu, X. Xia, J. Tu, Directional construction of vertical nitrogen-doped ¹T–²H MoSe₂/graphene shell/core nanoflake arrays for efficient hydrogen evolution reaction, *Adv. Mater.* 29 (2017), 1700748, <https://doi.org/10.1002/adma.201700748>.
- [8] M.H. Wu, J.T. Lee, Y.J. Chung, M. Srinivas, J.M. Wu, Ultrahigh efficient degradation activity of single- and few-layered MoSe₂ nanoflowers in dark by piezo-catalyst effect, *Nano Energy* 40 (2017) 369–375, <https://doi.org/10.1016/j.nanoen.2017.08.042>.
- [9] Y.J. Chung, C.S. Yang, J.T. Lee, G.H. Wu, J.M. Wu, Hydrogen evolution reaction: coupling effect of piezo-flexocatalytic hydrogen evolution with hybrid 1T- and 2H-phase few-layered MoSe₂ nanosheets, *Adv. Energy Mater.* 10 (2020), 2002082, <https://doi.org/10.1002/aenm.202002082>.
- [10] J. Zhang, Y. Chen, M. Liu, K. Du, Y. Zhou, Y. Li, Z. Wang, J. Zhang, 1T@2H-MoSe₂ nanosheets directly arrayed on Ti plate: an efficient electrocatalytic electrode for hydrogen evolution reaction, *Nano Res* 11 (2018) 4587–4598, <https://doi.org/10.1007/s12274-018-2040-x>.
- [11] J. Yan, Y. Zhang, Y. Huang, Y.-E. Miao, T. Liu, MoSe₂ nanosheets grown on polydopamine-derived porous fibers: a high-performance catalyst for hydrogen evolution reaction, *Adv. Mater. Interfaces* 4 (2017), 1600825, <https://doi.org/10.1002/admi.201600825>.
- [12] Y. Yu, G.-H. Nam, Q. He, X.-J. Wu, K. Zhang, Z. Yang, J. Chen, Q. Ma, M. Zhao, Z. Liu, F.-R. Ran, X. Wang, H. Li, X. Huang, B. Li, Q. Xiong, Q. Zhang, Z. Liu, L. Gu, Y. Du, W. Huang, H. Zhang, High phase-purity 1T'-MoSe₂-and 1T'-MoSe₂-layered crystals, *Nat. Chem.* 10 (2018) 638–643, <https://doi.org/10.1038/s41557-018-0035-6>.
- [13] S. Deng, C. Ai, M. Luo, B. Liu, Y. Zhang, Y. Li, S. Lin, G. Pan, Q. Xiong, Q. Liu, X. Wang, X. Xia, J. Tu, Coupled biphasic (¹T–²H)-MoSe₂ on mold spore carbon for advanced hydrogen evolution reaction, *Small* 15 (2019), 1901796, <https://doi.org/10.1002/smll.201901796>.
- [14] Y. Yin, Y. Zhang, T. Gao, T. Yao, X. Zhang, J. Han, X. Wang, Z. Zhang, P. Xu, P. Zhang, X. Cao, B. Song, S. Jin, Synergistic phase and disorder engineering in 1T-MoSe₂ nanosheets for enhanced hydrogen-evolution reaction, *Adv. Mater.* 29 (2017), 1700311, <https://doi.org/10.1002/adma.201700311>.
- [15] E.V. Calman, L.H. Fowler-Gerace, D.J. Choksy, L.V. Butov, D.E. Nikonov, I. A. Young, S. Hu, A. Mishchenko, A.K. Geim, Indirect excitons and trions in MoSe₂/WSe₂ van der Waals heterostructures, *Nano Lett.* 20 (2020) 1869–1875, <https://doi.org/10.1021/acs.nanolett.9b05086>.
- [16] Y. Li, R. Jia, H. Lin, X. Sun, F. Qu, Synthesis of MoSe₂/CoSe₂ nanosheets for NIR-enhanced chemodynamic therapy via synergistic in-situ H₂O₂ production and activation, *Adv. Funct. Mater.* 31 (2021), 2008420, <https://doi.org/10.1002/adfm.202008420>.
- [17] X. Zhang, Y.Y. Zhang, Y. Zhang, W.J. Jiang, Q.H. Zhang, Y.G. Yang, L. Gu, J.-S. Hu, L.J. Wan, Phase-controlled synthesis of 1T-MoSe₂/NiSe heterostructure nanowire arrays via electronic injection for synergistically enhanced hydrogen evolution, *Small Methods* 3 (2019), 1800317, <https://doi.org/10.1002/smt.201800317>.
- [18] S. Li, W. Zang, X. Liu, S.J. Pennycook, Z. Kou, C. Yang, C. Guan, J. Wang, Heterojunction engineering of MoSe₂/MoS₂ with electronic modulation towards synergistic hydrogen evolution reaction and supercapacitance performance, *Chem. Eng. J.* 359 (2019) 1419–1426, <https://doi.org/10.1016/j.cej.2018.11.036>.
- [19] D. Xiao, Q. Ruan, D.-L. Bao, Y. Luo, C. Huang, S. Tang, J. Shen, C. Cheng, P.K. Chu, Effects of ion energy and density on the plasma etching-induced surface area, edge electrical field, and multivacancies in MoSe₂ Nanosheets for enhancement of the hydrogen evolution reaction, *Small* 16 (2020), 2001470, <https://doi.org/10.1002/smll.202001470>.
- [20] J. Lee, C. Kim, K. Choi, J. Seo, Y. Choi, W. Choi, Y.-M. Kim, H.Y. Jeong, J.H. Lee, G. Kim, H. Park, In-situ coalesced vacancies on MoSe₂ mimicking noble metal: unprecedented Tafel reaction in hydrogen evolution, *Nano Energy* 63 (2019), 103846, <https://doi.org/10.1016/j.nanoen.2019.06.042>.
- [21] Y.S. Chang, C.Y. Chen, C.J. Ho, C.M. Cheng, H.R. Chen, T.Y. Fu, Y.T. Huang, S. W. Ke, H.Y. Du, K.Y. Lee, L.C. Chao, L.C. Chen, K.H. Chen, Y.W. Chen, R.S. Chen, Surface electron accumulation and enhanced hydrogen evolution reaction in MoSe₂ basal planes, *Nano Energy* 84 (2021), 105922, <https://doi.org/10.1016/j.nanoen.2021.105922>.
- [22] Z. Mao, C. Wang, H. Lu, K. Tang, Q. Li, C. Yan, X. Wang, Boron-modified electron transfer in metallic 1T MoSe₂ for enhanced inherent activity on per-catalytic site toward hydrogen evolution, *Adv. Mater. Interfaces* 7 (2020), 1901560, <https://doi.org/10.1002/admi.201901560>.
- [23] Y. Huang, Y. Sun, X. Zheng, T. Aoki, B. Pattengale, J. Huang, X. He, W. Bian, S. Younan, N. Williams, J. Hu, J. Ge, N. Pu, X. Yan, X. Pan, L. Zhang, Y. Wei, J. Gu, Atomically engineering activation sites onto metallic 1T-MoS₂ catalysts for enhanced electrochemical hydrogen evolution, *Nat. Commun.* 10 (2019) 982, <https://doi.org/10.1038/s41467-019-08877-9>.
- [24] C. Jian, Q. Cai, W. Hong, J. Li, W. Liu, Edge-riched MoSe₂/MoO₂ hybrid electrocatalyst for efficient hydrogen evolution reaction, *Small* 14 (2018), 1703798, <https://doi.org/10.1002/smll.201703798>.
- [25] Z. Sun, Y. Wang, L. Zhang, H. Wu, Y. Jin, Y. Li, Y. Shi, T. Zhu, H. Mao, J. Liu, C. Xiao, S. Ding, Simultaneously realizing rapid electron transfer and mass transport in jellyfish-like Mott-Schottky nanoreactors for oxygen reduction reaction, *Adv. Funct. Mater.* 30 (2020), 1910482, <https://doi.org/10.1002/adfm.201910482>.
- [26] X.-H. Li, M. Antonietti, Metal nanoparticles at mesoporous N-doped carbons and carbon nitrides: functional Mott-Schottky heterojunctions for catalysis, *Chem. Soc. Rev.* 42 (2013) 6593–6604, <https://doi.org/10.1039/C3CS60067J>.
- [27] N. Cheng, S. Stambula, D. Wang, M.N. Banis, J. Liu, A. Riese, B. Xiao, R. Li, T.-K. Sham, L.-M. Liu, G.A. Botton, X. Sun, Platinum single-atom and cluster catalysis of the hydrogen evolution reaction, *Nat. Commun.* 7 (2016) 13638, <https://doi.org/10.1038/ncomms13638>.
- [28] X. He, Y. Deng, Y. Zhang, Q. He, D. Xiao, M. Peng, Y. Zhao, H. Zhang, R. Luo, T. Gan, H. Ji, D. Ma, Mechanochemical kilogram-scale synthesis of noble metal single-atom catalysts, *Cell Rep. Phys. Sci.* 1 (2020), 100004, <https://doi.org/10.1016/j.xcrp.2019.100004>.
- [29] W. Wu, L. Wang, Y. Li, F. Zhang, L. Lin, S. Niu, D. Chenet, X. Zhang, Y. Hao, T. F. Heinz, J. Hone, Z.L. Wang, Piezoelectricity of single-atomic-layer MoS₂ for energy conversion and piezotronics, *Nature* 514 (2014) 470–474, <https://doi.org/10.1038/nature13792>.
- [30] S.K. Kim, R. Bhatia, T.H. Kim, D. Seol, J.H. Kim, H. Kim, W. Seung, Y. Kim, Y. H. Lee, S.-W. Kim, Directional dependent piezoelectric effect in CVD grown monolayer MoS₂ for flexible piezoelectric nanogenerators, *Nano Energy* 22 (2016) 483–489, <https://doi.org/10.1016/j.nanoen.2016.02.046>.
- [31] J.M. Wu, W.E. Chang, Y.T. Chang, C.-K. Chang, Piezo-catalytic effect on the enhancement of the ultra-high degradation activity in the dark by single- and few-layers MoS₂ nanoflowers, *Adv. Mater.* 28 (2016) 3718–3725, <https://doi.org/10.1002/adma.20105785>.
- [32] Y.T. Lin, S.N. Lai, J.M. Wu, Simultaneous piezoelectrocatalytic hydrogen-evolution and degradation of water pollutants by quartz microrods/few-layered MoS₂ hierarchical heterostructures, *Adv. Mater.* 32 (2020), 202002875, <https://doi.org/10.1002/adma.202002875>.
- [33] C.-Y. Tu, J.M. Wu, Localized surface plasmon resonance coupling with piezophotonic effect for enhancing hydrogen evolution reaction with Au@MoS₂ nanoflowers, *Nano Energy* 87 (2021), 106131, <https://doi.org/10.1016/j.nanoen.2021.106131>.
- [34] Y.C. Wang, J.M. Wu, Effect of controlled oxygen vacancy on H₂-production through the piezocatalysis and piezophotonics of ferroelectric R3C ZnSnO₃ nanowires, *Adv. Funct. Mater.* 30 (2020), 1907619, <https://doi.org/10.1002/adfm.201907619>.
- [35] X. Gao, Y. Chen, T. Sun, J. Huang, W. Zhang, Q. Wang, R. Cao, Karst landform-featured monolithic electrode for water electrolysis in neutral media, *Energy Environ. Sci.* 13 (2020) 174–182, <https://doi.org/10.1039/C9EE02380A>.
- [36] Z. Zhuang, Q. Peng, J. Zhuang, X. Wang, Y. Li, Controlled hydrothermal synthesis and structural characterization of a nickel selenide series, *Chem. Eur. J.* 12 (2006) 211–217, <https://doi.org/10.1002/chem.200500724>.
- [37] Y. Qu, H. Medina, S.W. Wang, Y.C. Wang, C.W. Chen, T.Y. Su, A. Manikandan, K. Wang, Y.C. Shih, J.W. Chang, H.C. Kuo, C.Y. Lee, S.Y. Lu, G. Shen, Z.M. Wang, Y. L. Chueh, Wafer scale phase-engineered 1T- and 2H-MoSe₂/Mo core-shell 3D-hierarchical nanostructures toward efficient electrocatalytic hydrogen evolution reaction, *Adv. Mater.* 28 (2016) 9831–9838, <https://doi.org/10.1002/adma.201602697>.
- [38] M. Jiang, J. Zhang, M. Wu, W. Jian, H. Xue, T.W. Ng, C.S. Lee, J. Xu, Synthesis of 1T-MoSe₂ ultrathin nanosheets with an expanded interlayer spacing of 1.17 nm for efficient hydrogen evolution reaction, *J. Mater. Chem. A* 4 (2016) 14949–14953, <https://doi.org/10.1039/C6TA07020E>.
- [39] L.J. Yang, Y.Q. Deng, X.F. Zhang, H. Liu, W.J. Zhou, MoSe₂ nanosheet/MoO₂ nanobelt/carbon nanotube membrane as flexible and multifunctional electrodes for full water splitting in acidic electrolyte, *Nanoscale* 10 (2018) 9268–9275, <https://doi.org/10.1039/C8NR01572D>.
- [40] S. Deng, F. Yang, Q. Zhang, Y. Zhong, Y. Zeng, S. Lin, X. Wang, X. Lu, C.Z. Wang, L. Gu, X. Xia, J. Tu, Phase modulation of (¹T–²H)-MoSe₂/TiC-C shell/core arrays via nitrogen doping for highly efficient hydrogen evolution reaction, *Adv. Mater.* 30 (2018), 1802223, <https://doi.org/10.1002/adma.201802223>.
- [41] L. Li, B. Wang, G. Zhang, G. Yang, T. Yang, S. Yang, S. Yang, Electrochemically modifying the electronic structure of IrO₂ nanoparticles for overall electrochemical water splitting with extensive adaptability, *Adv. Energy Mater.* 10 (2020), 2001600, <https://doi.org/10.1002/aenm.202001600>.
- [42] F. Luo, L. Guo, Y. Xie, J. Xu, K. Qu, Z. Yang, Iridium nanorods as a robust and stable bifunctional electrocatalyst for pH-universal water splitting, *Appl. Catal. B Environ.* 279 (2020), 119394, <https://doi.org/10.1016/j.apcatb.2020.119394>.
- [43] N.K. Oh, C. Kim, J. Lee, O. Kwon, Y. Choi, G.Y. Jung, H.Y. Lim, S.K. Kwak, G. Kim, H. Park, In-situ local phase-transitioned MoSe₂ in La_{0.5}Sr_{0.5}CoO₃-δ heterostructure and stable overall water electrolysis over 1000 hours, *Nat. Commun.* 10 (2019) 1723, <https://doi.org/10.1038/s41467-019-09339-y>.
- [44] L. Najafi, S. Bellani, R. Oropesa-Núñez, A. Ansaldo, M. Prato, A.E.D.R. Castillo, F. Bonaccorso, Engineered MoSe₂-based heterostructures for efficient

- electrochemical hydrogen evolution reaction, *Adv. Energy Mater.* 8 (2018), 1703212, <https://doi.org/10.1002/aenm.201703212>.
- [45] S. Geng, Y. Liu, Y.S. Yu, W. Yang, H. Li, Engineering defects and adjusting electronic structure on S doped MoO₂ nanosheets toward highly active hydrogen evolution reaction, *Nano Res.* 13 (1) (2020) 121–126, <https://doi.org/10.1007/s12274-019-2582-6>.
- [46] Y. Lu, C.L. Dong, Y.C. Huang, Y. Zou, Z. Liu, Y. Liu, Y. Li, N. He, J. Shi, S. Wang, Identifying the geometric site dependence of spinel oxides for the electrooxidation of 5-hydroxymethylfurfural, *Angew. Chem. Int. Ed.* 59 (2020) 19215–19221, <https://doi.org/10.1002/ange.202007767>.
- [47] X. Chia, M. Pumera, Characteristics and performance of two-dimensional materials for electrocatalysis, *Nat. Catal.* 1 (2018) 909–921, <https://doi.org/10.1038/s41929-018-0181-7>.
- [48] S. Dresch, F. Dionigi, M. Klingenhof, P. Strasser, Direct electrolytic splitting of seawater: opportunities and challenges, *ACS Energy Lett.* 4 (2019) 933–942, <https://doi.org/10.1021/acseenergylett.9b00220>.
- [49] Y. Li, Y. Zhang, X. Tong, X. Wang, L. Zhang, X. Xia, J. Tu, Recent progress on the phase modulation of molybdenum disulphide/diselenide and their applications in electrocatalysis, *J. Mater. Chem. A* 9 (2021) 1418–1428, <https://doi.org/10.1039/D0TA08514F>.
- [50] G. Wang, W. Chen, G. Chen, J. Huang, C. Song, D. Chen, Y. Du, C. Li, K.K. Ostrikov, Trimetallic Mo-Ni-Co selenides nanorod electrocatalysts for highly-efficient and ultra-stable hydrogen evolution, *Nano Energy* 71 (2020), 104637, <https://doi.org/10.1016/j.nanoen.2020.104637>.